Article

Performance Evaluation of Solar Still in Veracruz, Mexico Gulf Coastline

Jhon Jairo Feria-Díaz [1,2], María Cristina López-Méndez [1,*], Lucero Ortiz-Monterde [1], Boris A. Médina-Salgado [1,2] and Norma C. Perez-Rosas [3]

1 División de Estudios Posgrado e Investigación, Tecnológico Nacional de México/Instituto Tecnológico Superior de Misantla, Misantla 93821, Mexico; jhon.feria@unisucre.edu.co (J.J.F.-D.); 212t0019@itsm.edu.mx (L.O.-M.); boris.medina@unisucre.edu.co (B.A.M.-S.)
2 Facultad de Ingeniería, Universidad de Sucre, Sincelejo 700001, Colombia
3 School of Mechanical Engineering, Purdue University, West Lafayette, IN 47907, USA; nperezro@purdue.edu
* Correspondence: mclopezm@itsm.edu.mx

Abstract: Access to freshwater for rural populations is increasingly difficult worldwide. Even in coastal regions with abundantly available seawater, this is not suitable to meet the population's basic needs. Desalination with solar stills represents a simple, inexpensive, and accessible alternative to obtaining freshwater. This research shows the results obtained with a mathematical model of a single slope solar still proposed by Dunkle, compared with experimental data. Field experiments were carried out in the coastal zone of the Gulf of Mexico to validate the mathematical model. Different operating parameters of the solar still and their performance depending on climatic variations of the study site were studied. The average yield of distilled water was 1.57 L/m^2 d.

Keywords: solar still; desalination; mathematical model; solar radiation; Veracruz-Mexico

1. Introduction

Population growth, industrialization, and the fast growth of the agricultural sector have led to intensive water use and the contamination of water resources, resulting in less and less available water [1]. In addition, because of climate change, the planet is currently undergoing a significant freshwater shortage that affects almost 20% of the world's population [2,3]. Moreover, demand for freshwater is expected to increase to 6.9 trillion m^3 by 2030, representing an increase of more than 53% compared to the current level [4]. This change will undoubtedly aggravate the scarcity issue the planet has today. This scenario is very noticeable in populations settled in remote and rural areas, mainly in developing countries [5], as well as in coastal populations where seawater has very high salinities that range from 35,000 to 40,000 ppm, making it unsuitable for direct consumption [1].

As a solution to abstract freshwater, the desalination of seawater, brackish water, or groundwater is recommended [6]. A strategy proposed by the General Assembly of the United Nations to achieve the sixth goal of the Millennium Development Goals (SDG) [7] has to do with international cooperation and the creation of technological infrastructure in developing countries for water desalination.

Desalination has been known throughout history, both as a concept and technology. Generally, in the past, and specifically, during the times of ancient China (475–221 BC) [8] and Aristotle (384–322 BC) [9], the possibility of desalination through evaporation and subsequent condensation was already known, and the technique was widely used by sailors. Before the Industrial Revolution, desalination was used mainly on transoceanic ships that needed to be supplied with freshwater. Nonetheless, it was only after WWII that major research was carried out in the US to improve desalination technologies [10].

Water desalination processes can be generally classified into phase change or thermal processes, and processes without phase change or using membranes [11–14]. The thermosolar water desalination method within the thermal desalination techniques is essentially

divided into the following two main categories: (a) direct systems and (b) indirect systems. The key difference between these desalination methods is that in the direct system, solar radiation is absorbed and converted into heat during the evaporation process of the saltwater inside the device, while in the indirect system, separate dual systems are used, i.e., a matrix for solar collection comprising of thermal and/or photovoltaic (PV) collectors, and a discrete conventional distillation plant to eliminate latent heat condensation loss [15].

Solar stills are direct system thermal devices, i.e., they absorb solar radiation and transform it into heat to evaporate saltwater, and then condense it inside the same device. They generally consist of an insulated black container where saltwater is available at a shallow depth. The basin is covered with a hermetically sealed glass lid to reduce steam leakage. Saltwater absorbs solar radiation, heats up, and then evaporates. When air saturated with vapor comes into contact with the fresh inner surface of the clear glass cover, some of the vapor molecules condense. This condensed water slides downward, where it is collected in a channel along the underside of the glass cover before moving through a plastic tube outside the tank. The maximum efficiency of a conventional solar still is generally around 50% in the case of total isolation. Less insulation causes an efficiency reduction of approximately 14.5% [16].

Many factors can affect solar still productivity, such as temperature differences between glass and saltwater basins, basin area, glass cover inclination, device orientation, materials used in manufacture, and local climatic conditions [1,16]. In essence, the productivity of a conventional solar still depends mainly on the climatic conditions of the site where the device is installed, the operating parameters, and the design parameters [16–18].

Although solar stills are simple structures, various researchers have gone to great lengths to model the heat and mass transfer phenomena that occur inside. Thermal modeling is very important, since based on theoretical results, the thermal behavior of the solar still can be researched, and a parametric study can be carried out to optimize the system without the need to manufacture it [6].

The first mathematical model proposed for a solar still was the one reported by Dunkle in 1961 [19], where he introduced heat and mass transfer equations for a conventional desalinator based on thermal circuit diagrams. Despite its constraints, this model is the most popular, and it is still used by most researchers in the solar distillation field. Other popular models are those proposed by Chen et al. (1984) and by Clark et al. (1990) to evaluate the heat transfer coefficient [20]. Nonetheless, Kumar and Tiwari's works (1996) allowed them to formulate a more realistic mathematical model of these heat transfer coefficients for a higher range of water temperatures, based on a linear regression analysis [21]. Likewise, Adhikari et al. (1990) suggested a mathematical expression to estimate the production of distilled water per hour in the solar still as a function of the vapor pressures and temperatures of the water and glass cover [22].

The main objective of this research study is to verify the performance of a solar still under the climatic conditions from the coast of the Gulf of Mexico, in addition to finding out the design's influence and operation parameters in freshwater abstraction. Similarly, the effectiveness of a mathematical model and the associated kinetic coefficients are verified, which allows for the simulation of real field conditions.

Main Hydrological Characteristics of Mexico

Mexico is located between meridians 118°22′00″ and 86°42′36″ of West longitude and between 14°32′27″ and 32°43′06″ North latitude. The country has a rugged topographic relief with a continental extension of 1,959,248 Km². It has a great variety of climates. The northwest and center of the country, which covers two-thirds of the territory, are considered arid or semi-arid areas, with an annual rainfall of less than 500 mm. In contrast, the southeast is humid, with average rainfall sometimes exceeding 2000 mm per year. During the 1981–2010 period, the country's average rainfall was 740 mm per year. According to the precipitation estimation from 1981 to 2010, Mexico receives about 1,449,471 m³ of water in precipitation form. With the latest hydrological calculations available for 2017, it is

estimated that 72.15% of water evapotranspires and returns to the atmosphere, 24.77% runs through rivers and streams, and the remaining 6.38% infiltrates and recharges the aquifers. Nonetheless, renewable water per capita nationwide is expected to decline from 3692 m^3 per capita year to 3250 m^3 by 2030, due to population growth. Although Mexico experiences a low degree of pressure on available water resources (19.5%) at the national level, there are areas of the country with a high degree of stress on the water, such as the one located in the Valley of Mexico, which experiences stress of around 141.4%. Similarly, there are densely populated regions in the Mexican state of Veracruz with high levels of social marginality which exert heavy pressure on water resources [23]. In addition, if only the demographic effects are considered, according to the Falkenmark water stress criterion, by 2030 most of the Mexican territory will be in water stress conditions (1000 to 1700 m^3/inhabit/year), scarcity (500 to 1000 m^3/inhabit/year), or absolute scarcity (<500 m^3/inhabit/year) [24].

2. Materials and Methods

2.1. Study Area Description

To obtain experimental data, field trials were conducted in La Guadalupe, Tecolutla-Veracruz, Mexico. The site coordinates are 20°22′26″ N and 97°4′55″ W. The rainy season is hot, oppressive, and mostly cloudy in Tecolutla. The dry season is hot, muggy, and with strong winds and partially overcast skies. Figure 1 shows the average pattern of radiation, temperature, relative humidity, and cloudiness throughout the year in Tecolutla (data obtained from the "General Heriberto Jara" climatological station located in the Veracruz International Airport).
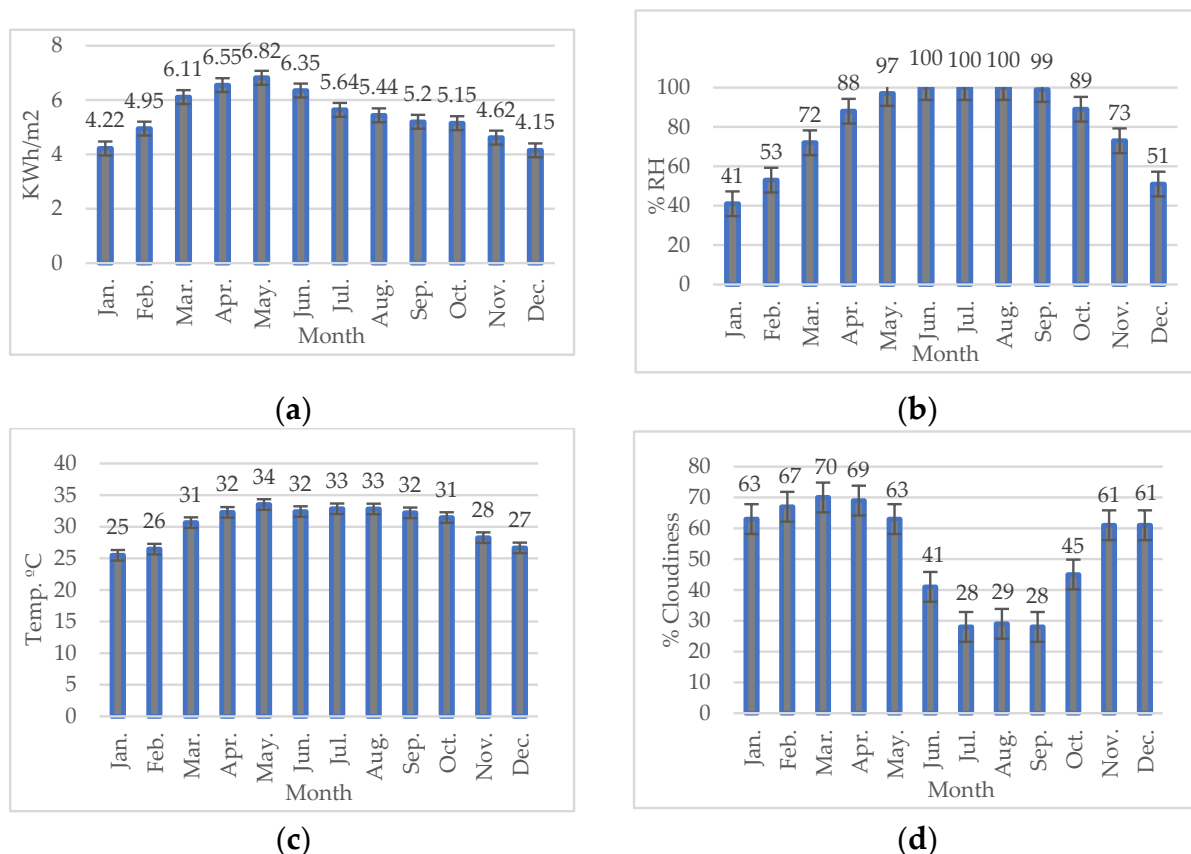

Figure 1. Average annual climatic behavior in Tecolutla, Mexico. (**a**) Solar radiation, (**b**) Relative humidity, (**c**) Ambient temperature, and (**d**) Cloudiness. The figures show the monthly average behavior of each parameter and indicate their respective values per month. (The figure includes standard error bars).

The most radiant time of the year in Tecolutla is between mid-March and June, with a daily average of solar energy per m^2 in excess of 6.3 kWh, whereas May is the brightest month of the year, with 6.82 kWh on average. The darkest month is December, with 4.15 kWh on average. Tecolutla has an extreme seasonal variation in humidity. The hottest period encompasses 9.6 months between late February and early December, in which the comfort level is sweltering, oppressive, or extremely humid at least 48% of the time. During the year, the temperature ranges from 18 to 32 °C, and is rarely below 14 °C or above 34 °C. The probability of rainy days in Tecolutla varies remarkably throughout the year. The season with the highest rainfall encompasses 4.4 months between June and October, with a more than 45% probability that it will rain on any given day. The month with the rainiest days in Tecolutla is September, with an average of 20.8 days with at least 1 mm of precipitation. The dry season lasts 7.6 months between October and June. The month with the fewest rainy days in Tecolutla is March, with an average of 5.4 days with at least 1 mm of precipitation. September is the month with the most rain-only days, with an average of 20.8 days.

Climatic factors such as the solar radiation intensity, wind speed, ambient temperature, relative humidity, and cloudiness directly influence the solar distillation productivity [16] and, considering that the region of Tecolutla in Mexico receives high solar radiation and presents conditions of relative humidity, ambient temperature, and cloudiness favorable to evaporation-condensation processes, these condition allow for the implementation and use of solar stills as a brackish water desalination system.

2.2. Field Trials and Statistical Data Management

Bearing in mind that cloudiness is a factor that directly affects the amount of solar radiation on the Earth's surface, it consequently reduces the performance of any solar distillation system [18,25]. Thus, we decided to carry out the monitoring in August. Tecolutla has high solar radiation, a high average temperature, and a low percentage of cloudiness during this month, as compared to other months. The monitoring of the solar prototype was performed between 23 and 28 August 2021. It is important to note that Hurricane Grace crossed the study area on 21 August that year. Therefore, we considered the influence of this storm in our analysis of the results. Field trials were carried out between 8:00 a.m. and 6:00 p.m. on each monitoring day, depending on the sunrise and sunset. With the obtained data, a statistical analysis of its variance was performed through ANOVA, using the trial version of the Statgraphics Centurion XVI software. The significance level was established for a *p*-value < 0.05 for all cases.

The base area (0.054 m^2) of the solar still prototype worked as a basin for the brackish seawater. The material with which the solar still was built was a glass covered by a black plastic film to conserve heat more efficiently inside the prototype. The solar still has a glass cover inclined at 40°, where the evaporated water is condensed in the heating container and then stored in a freshwater compartment inside the solar still. For the test, 1 L of seawater was placed in the heating tray through a lid located in the upper part of the still, and the distilled water was extracted through a hole located in the front part of the prototype. The system was sealed with silicone to prevent heat exchange from outside, as well as the entry of dust, polluting particles, or external water vapor. General dimensions of the solar still are shown in Figure 2.

Additionally, a basin with an area like the still basin worked as a control. A smart weather station, Ambient Weather brand, WS-2902C model, was used, with the capacity to measure solar radiation, relative humidity, ambient air temperature, wind direction, and speed in the field. A laser beam temperature meter and K-type thermocouples were used for the digital multimeter to measure the temperature both inside and outside the prototype and the control. Figure 3 shows the equipment used in the field monitoring.

(**a**) (**b**)

Figure 2. Solar still used in the field trials: (**a**) side view and (**b**) front view. The solar still is 0.50 m long and 0.30 m high and wide, respectively. The walls of the solar still were built in glass with a thickness of 5 mm and the water basin was in metal (area = 0.054 m^2). It was covered with black adhesive paper to improve the absorptivity of solar radiation and increase the internal heat of the solar still.
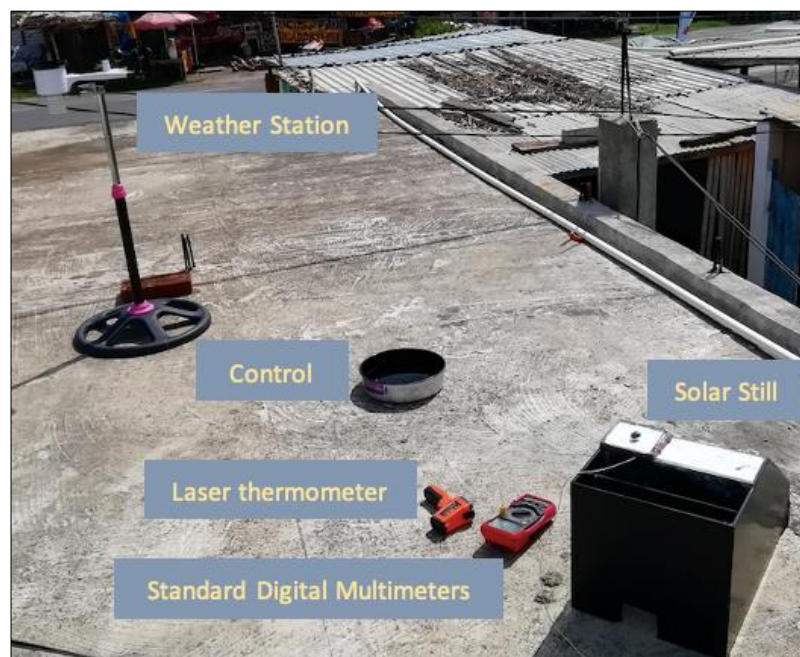

Figure 3. Equipment used for in-field monitoring. The instruments used in the monitoring are shown, including the control basin, the weather station, laser thermometer, multimeters, and the thermocouples installed in the solar still.

2.3. Proposed Mathematical Model for the Solar Still

For the solar still used in the tests, the mathematical model proposed was based on the original model from Dunkle [19]. Dunkle's model is important, since it clearly defines the coefficients of heat transfer by convection and evaporation, based on physical parameters that occur inside the solar still (the water and glass temperature). This model has also been widely used by other authors such as Jamil et al. (2021) [25], as well as Duffie and Beckman (2013) [26], and Antar et al. (2010) [27], who reported good simulation results.

Figure 4 shows the geometry and energy transfer mechanisms considered in this research study.
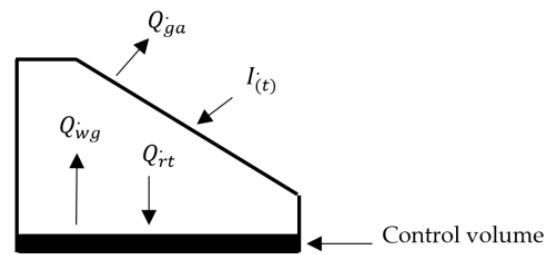

Figure 4. Initial energy balance in the solar still. The arrows indicate the direction of heat input and loss in the basin water (volume control) and in the glass cover of the solar still.

To perform the energy balance in the solar still, we considered the following assumptions [20], namely:

1. There were no steam leaks from the solar still.
2. Water mass in the solar distillation basin was presumed to be constant.
3. Water mass loss by evaporation was negligible.
4. The temperature gradient along the depth of the body of water was negligible.
5. The heat and absorption capacities were negligible, and the heat and absorption capacities for the cover glass and insulation material were also negligible.
6. The glass cover inclination concerning the horizontal was negligible.
7. The areas of the glass and water surfaces were similar to the surface of the container holding the seawater.

Figure 4 shows the energy balance from the solar still (see also Equation (1)).

$$Q^{\cdot} = Q_{rt}^{\cdot} - Q_{wg}^{\cdot} - Q_{ga}^{\cdot} \qquad (1)$$

In Equation (1) $Q^{\cdot}$ is the net heat of the system, $Q_{rt}^{\cdot}$ is the incident thermal radiation that reaches the water body, $Q_{wg}^{\cdot}$ is the total energy loss (heat by convection, evaporation, and radiation) from the water to the glass cover, and $Q_{ga}^{\cdot}$ is the energy loss (heat by convection and radiation) from the glass cover to the environment. Figure 5 shows a more detailed breakdown of the different elements that intervene in the general balance of the water mass, described in Equation (1).
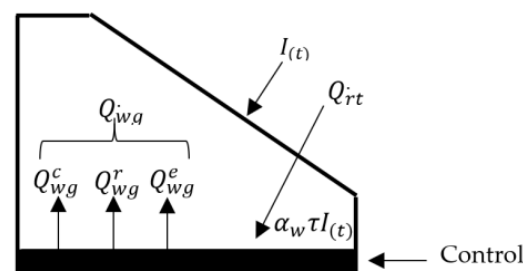

Figure 5. Energy transport mechanisms in a single-slope solar still. The figure shows the forms of heat loss from water to glass where steam condensation occurs.

In Figure 5, the incident thermal radiation $(Q_{rt}^{\cdot})$ is a function of the global radiation in the study area $I_{(t)}$ in W/m², water absorptivity (α_w, dimensionless), and glass transmissivity (τ, dimensionless), as indicated in the following Equation (2):

$$Q_{rt}^{\cdot} = \alpha_w \tau I_{(t)}, \qquad (2)$$

Contrastingly, the total energy loss from the water to the glass cover is as follows:

$$Q_{wg}^{\cdot} = Q_{wg}^{C} + Q_{wg}^{r} + Q_{wg}^{e}, \qquad (3)$$

where Q_{wg}^C is the heat transfer from the water to the glass cover by convection, Q_{wg}^r is the heat transfer from the water to the glass cover by radiation, and Q_{wg}^e is the heat transfer by evaporation, all in units of W/m². Equations (4)–(6) show each of these heat transfers as follows:

$$Q_{wg}^C = h_c (T_w - T_g). \tag{4}$$

Here, h_c is the convection heat transfer coefficient (W/m² °C), and T_w and T_g are the water and the glass temperatures measured in °C, respectively.

$$Q_{wg}^r = \varepsilon_{eff}\sigma \left[(T_w + 273)^4 - (T_g + 273)^4 \right]. \tag{5}$$

In Equation (5), ε_{eff} is the effective emissivity from the water surface to the glass cover, and σ is the Stefan–Boltzmann constant, equivalent to 5.67×10^{-8} W/m² K⁴ [28].

$$Q_{wg}^e = h_{ec} (T_w - T_g) \tag{6}$$

where h_{ec} is the heat transfer coefficient by evaporation between the water and the glass cover (W/m² °C) [28,29].

Conversely, considering that the net heat ($Q^{\cdot}$) is equal to the change in the internal energy of the system (U) as a time function, it is possible to propose an energy balance from a batch system in a non-isothermal state, particularly as follows:

$$Q^{\cdot} = \frac{dU}{dt} = \frac{d(m_w u)}{dt} = m_w \frac{du}{dt} + u\frac{dm_w}{dt} = m_w C_w \frac{dT_w}{dt} \tag{7}$$

In Equation (7), the term $\frac{dm_w}{dt}$ is null, since the change in water mass (m_w) is a function of time, i.e., the evaporation rate is low and negligible according to the assumptions made for the model. Equalizing Equations (1) and (7), and if Q_{ga} is neglected, since it does not directly intervene in the water condensation process, we have the following:

$$Q^{\cdot} = Q_{rt} - Q_{wg} = m_w C_w \frac{dT_w}{dt}, \tag{8}$$

Here, C_w represents the water-specific heat and T_w represents the water temperature. If Equation (2) is replaced in Equation (8), and the result is left as a function of the incident thermal radiation, we can rewrite the differential equation. So, it follows that:

$$\alpha_w \tau I_{(t)} = m_w C_w \frac{dT_w}{dt} + Q_{wg} \tag{9}$$

To this extent, the energy and mass balance of water can be described as the energy absorbed from solar radiation = the energy stored + the energy lost to the glass inner surface by convection, evaporation, and radiation [20]. Equation (9) represents the differential equation of the energy balance on the water in the basin (and on the basin itself), per unit area of the basin [26].

To estimate the heat transfer coefficient by natural convection h_c, radiation h_r, and evaporation h_{ec} between the water mass and the inner surface of the glass cover, the following equations proposed by Dunkle can be used [20,26–31]:

$$h_c = 0.884 \times \left[(T_w - T_g) + \frac{(P_w - P_g)(T_w + 273.15)}{268.9 \times 10^3 - P_w} \right]^{\frac{1}{3}}, \tag{10}$$

$$h_r = \frac{\varepsilon_{eff}\sigma \left[(T_w + 273)^4 - (T_g + 273)^4 \right]}{(T_w - T_g)}, \tag{11}$$

$$h_{ec} = \frac{h_c \left(16.28 \times 10^{-3}\right) \left(P_w - P_g\right)}{\left(T_w - T_g\right)}. \tag{12}$$

The saturation vapor pressures at water temperature (P_w) and the temperature of the inner surface of the glass cover, in units of N/m^2, are evaluated using the following expressions [20,32]:

$$P_w = exp\left[25.317 - \left(\frac{5144}{T_w + 273}\right)\right], \tag{13}$$

$$P_g = exp\left[25.317 - \left(\frac{5144}{T_g + 273}\right)\right]. \tag{14}$$

Finally, the hourly distillate per unit basin area (M_w), daily distillate per unit basin area (M'_w), and efficiency of the solar still η are given by the following relations [29]:

$$M_w = h_{ec} \left(T_w - T_g\right) \times \frac{3600}{L_{ev}}, \tag{15}$$

$$M'_w = \sum_{i=1}^{24} M_w, \tag{16}$$

$$\eta = \frac{M'_w \times L_{ev}}{A_b \times \sum I_{(t)} \times \Delta t}. \tag{17}$$

where L_{ev} is the latent heat of vaporization of water (J/kg), A_b is the basin liner surface area of still (m^2), and Δt is the fraction of the day when the monitoring was performed.

2.4. Statistical Indicators for the Performance Evaluation of the Mathematical Model

The performance and statistical fit of the model were measured through the following five standard statistical metrics: absolute error (AE), percent relative error (PRE), correlation coefficient (R), determination coefficient (R^2), and mean absolute percent error (MAPE). Equations (18)–(22) define these performance measures [20,33–35] as follows:

$$AE = |y_i - q_i|. \tag{18}$$

$$PRE = \frac{AE}{y_i} \times 100. \tag{19}$$

$$R = \frac{\sum_{i=1}^{n}\left(y_i - y_i^-\right)\left(q_i - q_i^-\right)}{\sqrt{\sum_{i=1}^{n}\left(y_i - y_i^-\right)^2 \ \sum\left(q_i - q_i^-\right)^2}}. \tag{20}$$

$$R^2 = \left(\frac{\sum_{i=1}^{n}\left(y_i - y_i^-\right)\left(q_i - q_i^-\right)}{\sqrt{\sum_{i=1}^{n}\left(y_i - y_i^-\right)^2 \ \sum\left(q_i - q_i^-\right)^2}}\right)^2 \tag{21}$$

$$MAPE = \frac{1}{N}\sum_{i=1}^{n}\left|\frac{y_i - q_i}{y_i}\right| \times 100. \tag{22}$$

where y_i is the experimental value measured, and q_i corresponds to the predictive value of the model in the time interval "i". The values y_i^- and q_i^- are the averages of the measured and predicted values, respectively. N corresponds to the data number of "i".

The first two statistical indicators (Equations (18) and (19)) were used to measure the error between the experimental and predictive data of the model for each time interval, and the other three (Equations (20)–(22)), were used to evaluate the general fit of the predictive mathematical model with the experimental data found in the monitoring sessions. When R is greater than 0.8, the predictive and experimental values are highly correlated. Similarly, an R^2 close to 1 indicates that the model values fit very well and are close to the values found experimentally [33,36]. An R^2 of 0.65 to 0.75 indicates outstanding performance, while an R^2 of less than 0.50 indicates poor performance [34,37].

On the other hand, MAPE indicates how large the model's predictive errors are compared to the experimental values. Furthermore, it is the best indicator to classify the statistical model based on its performance. Using MAPE, the predictive performance of a model can be considered as follows: excellent ($0\% \leq$ MAPE $\leq 10\%$), good ($10\% <$ MAPE $\leq 20\%$), fair ($20\% \leq$ MAPE$< 50\%$), or inaccurate ($50\% \leq$ MAPE) [33,34].

3. Results and Discussion

3.1. Seawater in the Control Basin

To verify the seawater evaporation potential under the climatic conditions of the test site, a control basin with the same volume of water as that of the distiller was used, i.e., 1 L of seawater. Figure 6 shows temperature behavior in the seawater and the control basin walls, respectively.
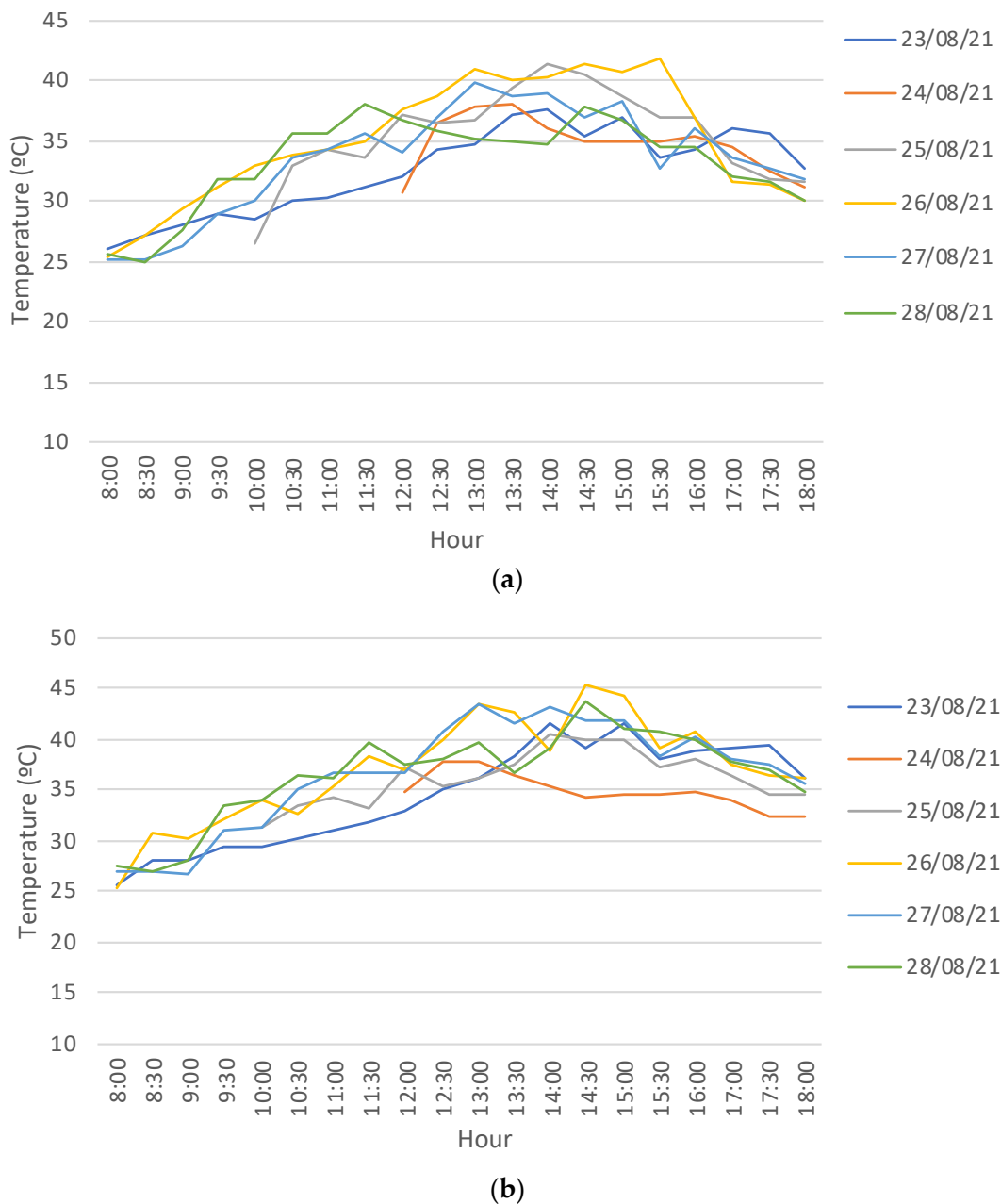

(a)

(b)

Figure 6. Temperature behavior in the control: (**a**) Water temperature and (**b**) Temperature of the control walls. The colors in the lines indicate the temperature of each monitored day.

After verifying the general fulfillment of the independence hypothesis, normality, and data homogeneity, an ANOVA was performed [38] to compare whether the mean temperatures of the seawater and the control exposed to solar radiation showed statistically significant differences between the different days monitored. *p*-values of 0.23 and 0.20 were found for the water temperature and walls inside the control, respectively. Considering that both values are greater than 0.05, it is possible to affirm thFigurasat there is no statistically significant difference between the mean temperatures of both seawater and the control, with a 95% confidence level [39], i.e., the behavior of these temperatures was very similar throughout the days monitored. The water temperature remained between 24.8 °C and 41.9 °C, while the control temperature was between 25.4 °C and 45.4 °C, with the highest temperatures occurring between 1:00 p.m. and 3:00 p.m.

The aforementioned results follow the climatic conditions expected in the month and at the site where the monitoring was carried out. The average rate of seawater evaporation in the control was 4.94 L/m^2-d. This value is higher than the reported rate of evaporation in tropical countries such as Indonesia, which is about 3.50 L/m^2-d [40]. This evaporation rate favors the solar still performance, characterized by low efficiencies (around 36%) [41]. Therefore, the higher the average evaporation rate of seawater under natural conditions, the higher the rate of distillation efficiency in the solar still.

3.2. Solar Radiation during Test Days

Solar radiation during the first days was affected by Hurricane Grace, which hit the region two days before the experiments started. Figure 7 shows solar radiation in the study area during the monitoring days.
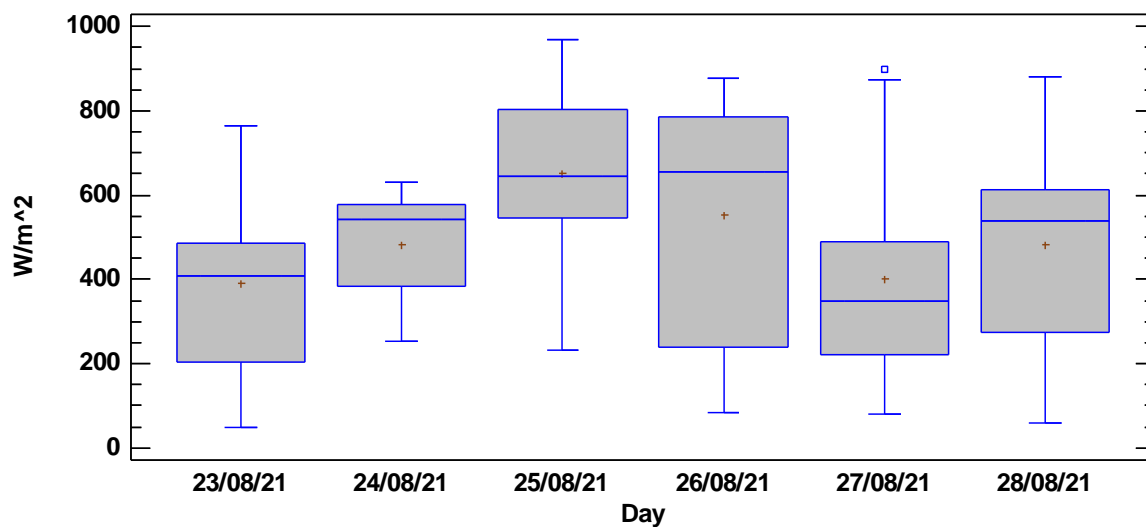

Figure 7. Solar radiation in the study area during test days. The central value of the box-and-whisker plot is the median of the data, the "+" represents the mean, and the lower and upper borders correspond to the first and third quartiles, respectively. Finally, the ends of the whiskers correspond to the minimum and maximum values of the analyzed data.

To verify if there are statistically significant differences in solar radiation among the days monitored, an ANOVA was used, previously checking the conditions of the data normality, independence, and homogeneity. A *p*-value equal to 0.009, less than 0.05, was found for the ANOVA, i.e., there is at least one statistically significant difference between the means of radiation between one or several days during the test, with a 95% confidence level. To determine which means are significantly different from others, the multiple range test was applied [39]. Table 1 shows the results obtained from Duncan's multiple range test, used to find significant differences between the means of solar radiation on the days monitored.

Table 1. Results of Duncan's multiple range test for mean solar radiation during the monitoring days.

Contrast	Significance	Difference	+/−Limits
23–24 August 2021		−89.8619	164.141
23–25 August 2021	*	−257.883	150.519
23–26 August 2021	*	−159.46	141.719
23–27 August 2021		−7.23524	141.719
23–28 August 2021		−90.4552	141.719
24–25 August 2021	*	−168.021	173.216
24–26 August 2021	*	−69.5983	165.627
24–27 August 2021		82.6267	165.627
24–28 August 2021		−0.593333	165.627
25–26 August 2021		98.4225	152.138
25–27 August 2021	*	250.647	152.138
25–28 August 2021	*	167.428	152.138
26–27 August 2021		152.225	143.437
26–28 August 2021		69.005	143.437
27–28 August 2021		−83.22	143.437

* Indicates a significant difference.

According to the results shown in Table 1, days 23, 24, and 25 have statistically significant differences from the rest of the days monitored, mainly due to the high cloudiness that occurred on 23 August and the rainfall in the morning of the 24th and 25th of that month. Consequently, it was decided to exclude days 24 and 25 from the ANOVA, since data were only recorded in the afternoon hours, after the rain events. Nonetheless, day 23 was included in the new ANOVA, because radiation data were recorded throughout that day. Correspondingly, 26–28 August were included. Table 2 shows the ANOVA results to compare the means of the selected days.

Table 2. ANOVA between the means of solar radiation on 23, 26, 27, and 28 August.

Source	Sum of Squares	DF	Mean Squares	F-Value	p-Value
Between Groups	346,691	3	115,564	1.96	0.127
Within Groups	4,539,740	77	58,957.6		
Total (Corr.)	4,886,430	80			

Because the p-value is greater than 0.05, there is no statistically significant difference among the mean solar radiation of the analyzed days, with a 95% confidence level. With this statistical certainty, an average solar radiation curve was constructed to include this factor in the proposed simulation model for the solar still. Figure 8 shows the average behavior of solar radiation during the monitored days.

3.3. Relative Humidity during Test Days

The relative humidity is the amount of water vapor in the air, expressed as a percentage of the amount needed to achieve saturation at a given pressure and temperature [42]. It has been shown that high levels of relative humidity in the environment favor the systemic performance of solar stills [43–45]. Figure 9 shows the relative humidity recorded at the monitoring site, during the test days.

When performing the ANOVA to verify differences between the means of relative humidity (%RH) from the different selected days, it was found that the data p-value was less than 0.05 (p-value = 0.0002), i.e., there is a statistically significant difference between the mean %RH for at least one day compared to the other days, with a 95.0% confidence level. Duncan's multiple range test was applied to identify which day or which days showed these differences. It was found that 23 August showed statistically significant differences in %RH with the other selected days. Table 3 shows the results of Duncan's multiple range test for %RH of the days considered.
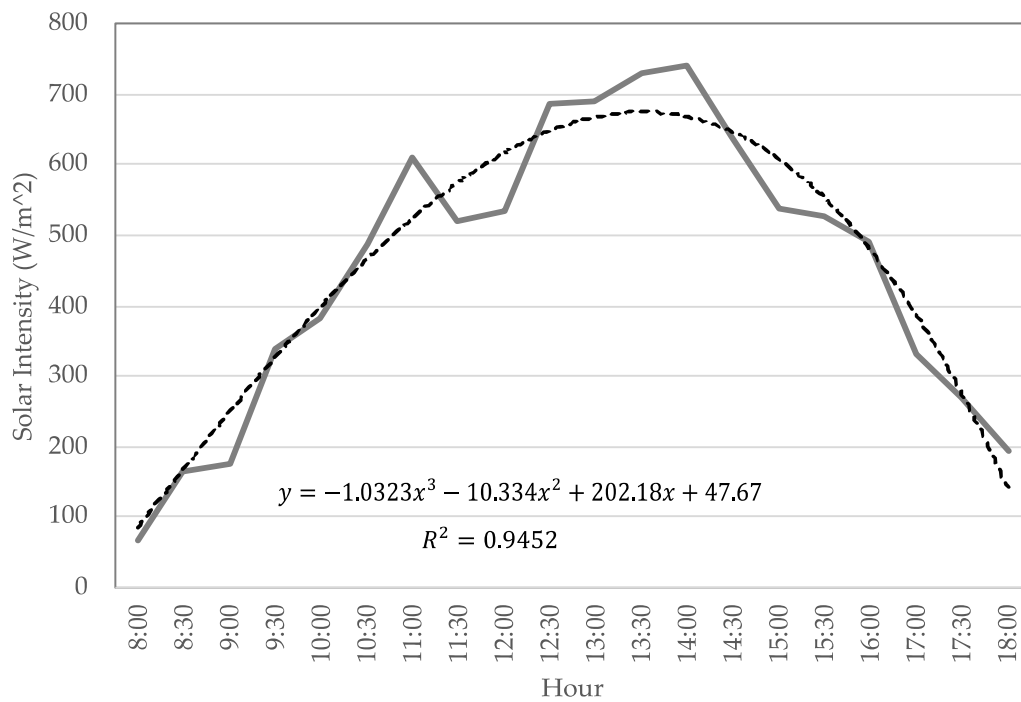
The equation shown in the figure:

$$y = -1.0323x^3 - 10.334x^2 + 202.18x + 47.67$$

$$R^2 = 0.9452$$

Figure 8. Average solar intensity during field trials. The continuous line represents the average experimental values of solar radiation, recorded every hour during the monitoring days. The dashed-dotted line represents the third-degree polynomial trend line of the experimental values, including the polynomial equation and its coefficient of determination R^2.
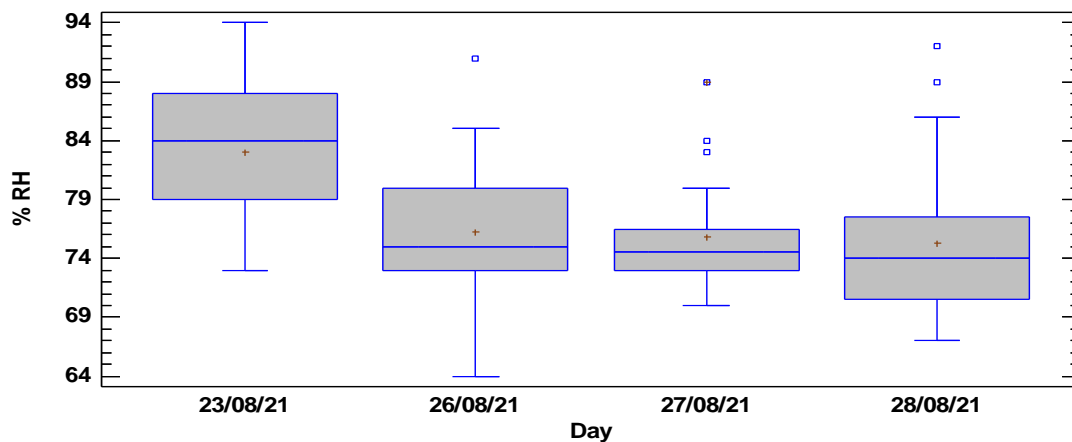

Figure 9. Relative humidity in the study area during the selected days of the test. The central value of the box-and-whisker plot is the median of the data, while the "+" represents the mean. The lower and upper borders correspond to the first and third quartiles, respectively. Finally, the ends of the whiskers correspond to the minimum and maximum values of the analyzed data.

Table 3. Results of Duncan's multiple range test for relative humidity means.

Contrast	Significance	Difference	+/−Limits
23–26 August 2021	*	6.74762	3.75432
23–27 August 2021	*	7.19762	3.75432
23–28 August 2021	*	7.74762	3.75432
26–27 August 2021		0.45	3.79983
26–28 August 2021		1.00	3.79983
27–28 August 2021		0.55	3.79983

* Indicates a significant difference.

Although on 23 August there was a higher %RH (between 73% and 94%) at the test site, higher than the other selected days, the solar still desalination rate was the lowest (0.56 L/m^2-d), contrary to expectations. This poor performance of the solar still could be due to the low solar radiation recorded that day, caused by the high cloud cover left after Hurricane Grace crossed the test site. Solar still efficiency is influenced by cloud cover, because it directly affects the amount of solar radiation absorbed by the solar still [46].

3.4. Temperatures in the Prototype and Ambiance

Temperatures were measured inside the solar still, at both seawater T_w and glass surface T_g where the condensation of the freshwater occurs. Additionally, the temperature in the external part of the glass T_{og} and the ambience T_a were recorded. Figure 10 shows a schematic of the places where these temperatures were taken using K-type thermocouples connected to a fluke-type data logger. Data were recorded every 30 min.
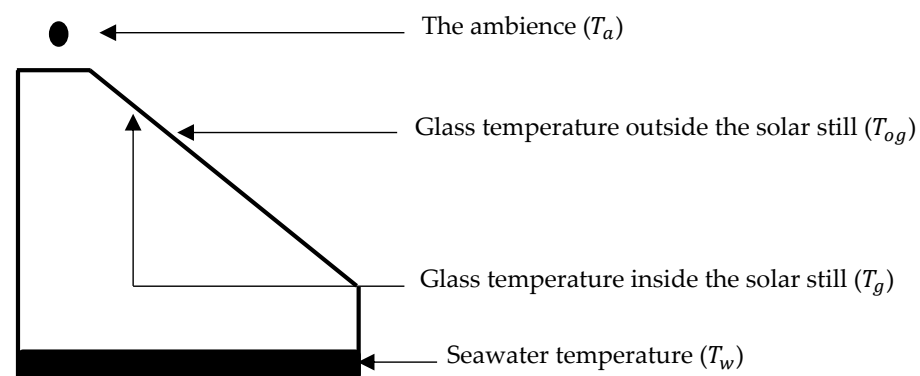

The ambience (T_a)

Glass temperature outside the solar still (T_{og})

Glass temperature inside the solar still (T_g)

Seawater temperature (T_w)

Figure 10. Location of the temperatures measured for the solar still tests. The location of the places where the temperature readings were taken using the thermocouples T_w and T_g and the laser thermometer T_{og} and T_a are shown.

Figure 11 shows the behavior of average temperatures, both inside and outside the prototype. For the selection of the days used to build this figure, an ANOVA, Duncan's multiple range tests, and the Kruskal–Wallis test were used to define on which days the temperatures showed statistically significant differences. It was found that the temperatures measured on 23 August showed significant differences with days 26, 27, and 28 from the same month, because the *p*-value of the data from the ANOVAs was greater than 0.05. In consequence, it was not considered. This is consistent with the behavior of relative humidity and solar radiation, as previously discussed.

The ambience in the morning hours was 25 °C, and it increased from 10:30 a.m. to values close to 30 °C. This temperature remained constant until the end of the day. By contrast, the other temperatures (T_w, T_g, T_{og}) had an ascending behavior in the morning hours, and a descending one at the end of the day, depending on the available solar radiation (see Figure 11). The highest temperature recorded corresponds to the water temperature, with values close to 45 °C, which reflects the heating capacity of the solar still. The internal temperature of the glass was much lower than the other temperatures reported, favoring the water vapor condensation inside the prototype.

3.5. Removal of Physicochemical Parameters during the Tests

The removal of some physicochemical parameters from seawater after desalination treatment with the prototype was evaluated. A Hanna instruments model HI98194 multiparametric meter was used to measure pH, salinity, dissolved oxygen, and total suspended Solids. Additionally, a Thermo Orion AQ 3010 digital Turbidimeter was used to measure turbidity.
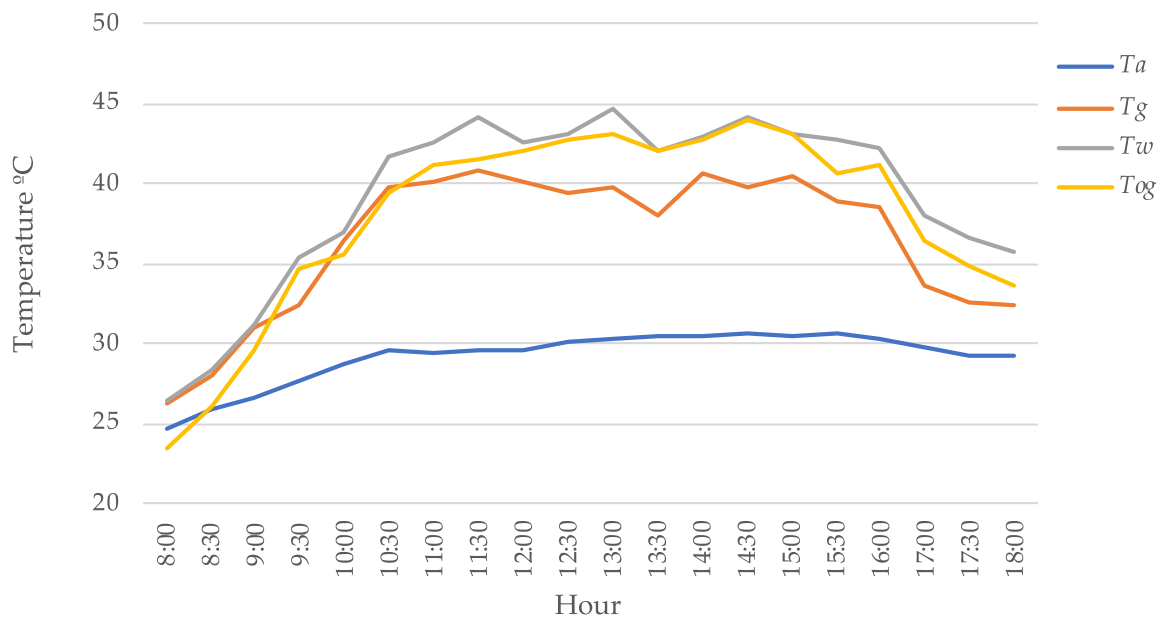
Figure 11. Average temperatures inside the prototype and in the ambience. The colors of the lines indicate the ambience (blue), glass temperature inside the solar still (red), water temperature in the basin (grey), and glass temperature outside the solar still (yellow).

Table 4 shows the physicochemical values of the water sample, before and after the solar desalination process.

Table 4. Physicochemical parameters of the sea and distilled water.

Water Quality Parameter	Seawater	Distillate Sample	Range *
pH	7.75	6.85	6.5–8.5
Dissolved oxygen (mg/L)	3.77	4.70	No guidance value set
Salinity (ppm)	2250	74.00	No guidance value set
Total Suspended Solids (mg/L)	1.62	0.0275	No guidance value set
Turbidity (NUT)	0.59	0.02	5.0
Fecal coliforms/*E. coli* (NMP/100 mL) **	Absence	Absence	Absence

* According to the standards of the World Health Organization [47]. ** It was made from the ISO 4832 method.

For the most part, the removal of salinity, turbidity, and total suspended solids was achieved in a high percentage (96.7%, 96.6%, and 98.3%, respectively), representing high viability in terms of water quality and the use of the solar still. Consistently, and following the drinking water quality standards from the World Health Organization, pH final values, turbidity, and fecal coliforms allow the direct consumption of the effluent water from the solar still after disinfection as a preventive sanitary measure, i.e., to avoid contamination after the distillation process.

3.6. Mathematical Model

The mathematical model used to simulate the theoretical values T_w is shown in Equation (9). Rewriting Equation (9) in terms of $\frac{dT_w}{dt}$ and substituting the values Q_{wg} from Equation (3), we obtain the following:

$$\frac{dT_w}{dt} = \left(\frac{1}{m_w C_w}\right)\left(\alpha_w \tau I_{(t)} - Q_{wg}^C - Q_{wg}^r - Q_{wg}^e\right). \qquad (23)$$

On the other hand, the following equations allow for the calculation of T_g, based on the solar intensity, T_w, and other parameters [20,29]:

$$T_g = \frac{\alpha'_g I_{(t)} + h^t_{wg} \times T_w + U^t_{ga} \times T_a}{h^t_{wg} + U^t_{ga}}, \tag{24}$$

$$\alpha'_g = (1 - R_g)\alpha_g, \tag{25}$$

$$h^t_{wg} = h_c + h_{ec} + h_r, \tag{26}$$

$$h^t_{ga} = 5.7 + 3.8v, \tag{27}$$

$$U^t_{ga} = \frac{\left(K_g/L_g\right) \times h^t_{ga}}{\left(K_g/L_g\right) + h^t_{ga}}. \tag{28}$$

where α_g is the thermal absorptivity of glass, α'_g is a fraction of solar flux absorbed by glass cover, R_g is the reflectivity of glass cover, h^t_{wg} is the total heat transfer coefficient from basin water to glass cover, h^t_{ga} is the total heat transfer coefficient from glass cover to ambience, v is the velocity in m/s, U^t_{ga} is the overall heat loss coefficient from glass cover inner surface to the atmosphere, K_g is the thermal conductivity glass, and L_g is the thickness of glass.

The Excel computer software was used to solve this differential equation and the others described in the Dunkle model by applying Euler's method. The results of the theoretical thermal model were then validated by comparing them with the experimental results obtained in this research study [29], considering the statistical indicators to measure the model fit.

Considering that T_w, T_g, h_c, and h_{ec} values in the solar still vary as a function of time, a numerical approach was used for their calculations, following the procedure described by Mowla et al. [48], as follows:

1. The initial heat transfer coefficients were estimated using the initial values of T_w and T_g, the specifications of the solar still, and other climatic parameters.
2. Knowing the heat transfer coefficients, the T_w for the following time interval was estimated using Euler's method to solve the derivative stated in Equation (23).
3. Using the new T_w value, T_g was calculated from Equation (24) and the heat transfer coefficients were calculated again, and step 2 was repeated for the other time interval, and so on.
4. During each time interval, T_w and T_g, heat transfer coefficients and climatic parameters were assumed to be constant, so the water evaporation rate was estimated for each time interval and, as a result, the total amount of freshwater production for that time interval was estimated.
5. For each time interval, the water amount in the basin was considered as the initial amount of water fed to the solar still minus the total amount of water evaporated up to that moment.

The set of design parameters and initial data to simulate the model are shown in Table 5.

Table 5. Physical input design parameters of the solar still prototype.

Parameters	Symbol	Value	Units	Reference
Initial basin water temperature	T_w	26.50	°C	-
Initial glass cover temperature	T_g	26.00	°C	-
Ambient temperature (average)	T_a	29.17	°C	-
Mass of water in the basin	m_w	1	Kg	-
Basin liner surface area of still	A_b	0.054	m^2	-
Velocity of wind (average)	v	3.0	m/s	-
Thickness of glass	L_g	0.005	m	-

Table 5. *Cont.*

Parameters	Symbol	Value	Units	Reference
Thermal absorptivity of water	α_w	0.30	Dimensionless	[28,29]
Thermal absorptivity of glass	α_g	0.05	Dimensionless	[28,29]
Fraction of solar flux absorbed by a glass cover	α'_g	0.0475	Dimensionless	[28,29]
Reflectivity of the glass cover	R_g	0.05	Dimensionless	[28,29]
Glass transmissivity	τ	0.90	Dimensionless	[28]
Heat capacity of water	C_w	4180	J/Kg °C	[29]
Stefan–Boltzmann constant	σ	5.67×10^{-8}	W/m^2 K^4	[29]
Latent heat of vaporization of water	L_{ev}	2,264,300	J/Kg	[29]
Effective emissivity between the water surface and the glass	ε_{eff}	0.90	Dimensionless	[49]
Thermal conductivity glass (average)	K_g	0.780	W/m °C	[50]
Time interval for Euler's method (Step size)	Δt	0.10	Hours	[48]

Figure 12 shows the results for theoretical T_w, obtained by the model and the experimental data found in the field.
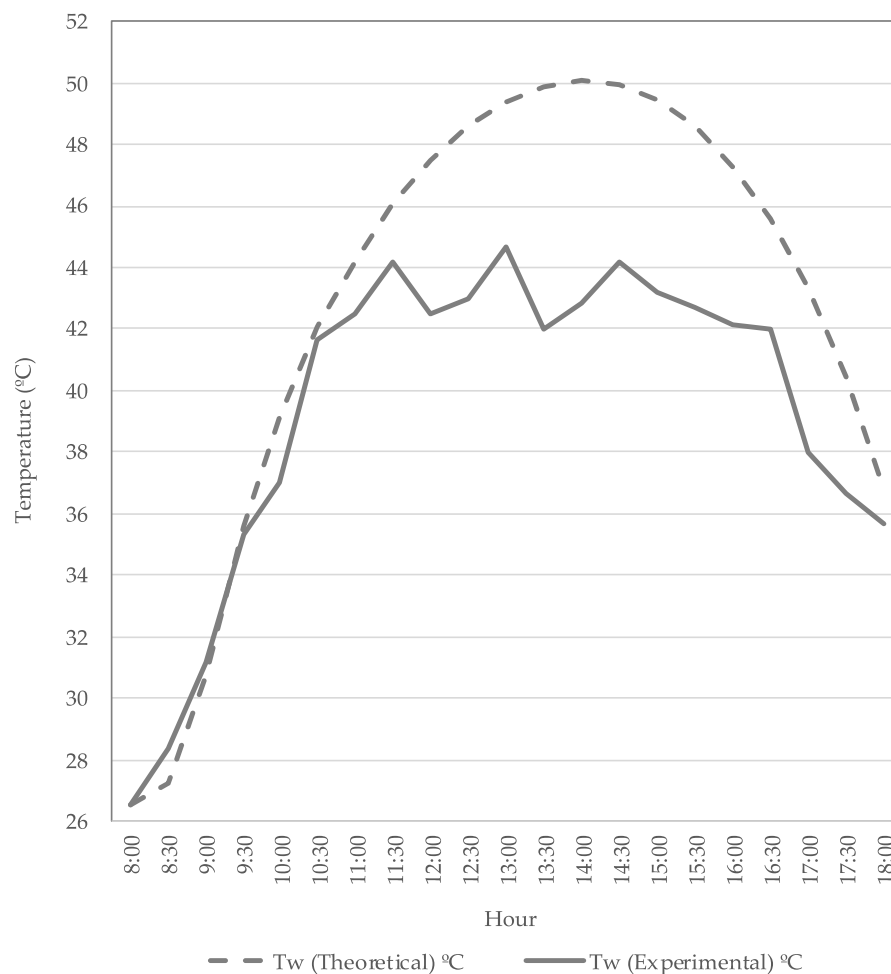

Figure 12. Comparison of experimental and theoretical results. The continuous line represents the average experimental values of water temperature recorded every hour during the monitoring days. The dashed-dotted line represents the theoretical values found with the model proposed by Dunkle.

Table 6 shows the results of the statistical indicators used to evaluate the closeness of fit of the T_w theoretical curve, found with the mathematical model, compared with the experimental data of T_w.

Table 6. Results of the statistical indicators used to evaluate the general adjustment of the model.

Statistical Metrics	Symbol	Value	Units
Correlation Coefficient	R	0.967	Dimensionless
Determination Coefficient	R^2	0.935	Dimensionless
Mean Absolute Percent Error	MAPE	8.646	Percent (%)

According to the statistical metrics shown in Table 6, the T_w theoretical model adequately and accurately predicts the real values of water temperature. The estimated R of 0.967 indicates that the predictive and experimental values are highly correlated, and that the R^2 of 0.935 shows that the model values fit very well and are close to the T_w experimental values. Contrastingly, MAPE of 8.646% suggests that the predictive performance of the model can be considered excellent ($0\% \leq \text{MAPE} \leq 10\%$). Nevertheless, when the statistical metrics of absolute error (AE) and percent relative error (PRE) are applied to each measure of time, there are two clearly defined intervals. The first interval comprises from 8:00 a.m. to 11:30 a.m., with a PRE of between 0.73% and 5.81%, indicating an excellent fit of the model with the experimental data. A second time interval is between 11:30 a.m. and 5:30 p.m., with a PRE of between 8.52% and 18.81%, showing a good fit but not as good as that of the previous intervals. Finally, between 5:30 p.m. and 6:00 p.m., a PRE of 3.26% was found, which indicates good proximity between the model and the final experimental data recorded. The time intervals where the bias of the model was greater may be due to the site climatic conditions during the days in which the tests were carried out, especially due to the influence of the high cloudiness and the occurrence of Hurricane Grace in the study area during the days before the tests.

Figure 13 shows the hourly variation of the heat transfer coefficients according to the results found in the simulation of the mathematical model.
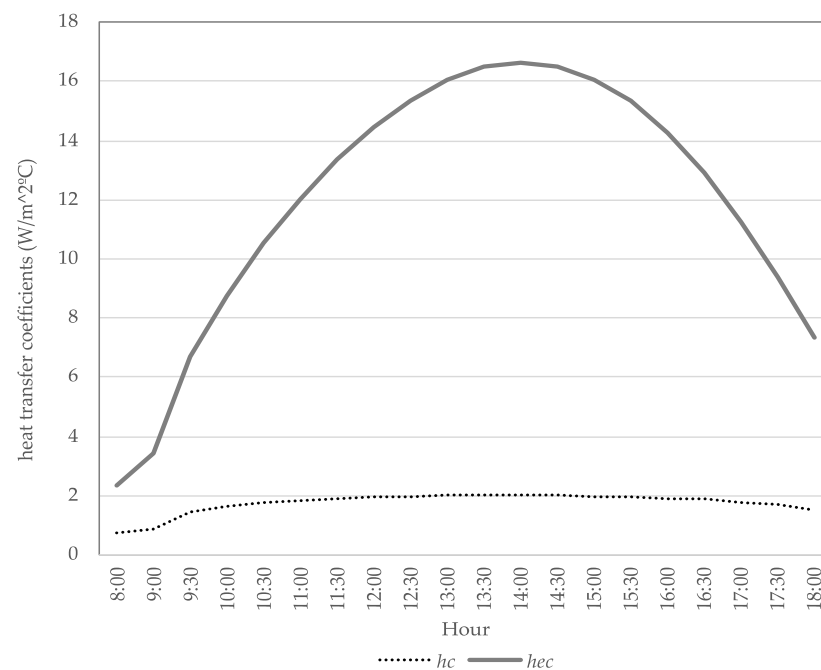

Figure 13. Hourly variation of heat transfer coefficients of basin water to glass. The continuous line represents the evaporation heat transfer coefficients (h_{ec}) and the dashed-dotted line represents the convective heat transfer coefficients (h_c).

The technical literature for solar stills has reported values for the convective (h_c) and evaporative (h_{ec}) heat transfer coefficients in a range of 1.65 to 2.58 W/m^2 °C and 8.00 to 35.00 W/m^2 °C, respectively [51]. According to Figure 13, values estimated by the mathematical model for h_c are between 0.75 to 2.01 W/m^2 °C, while for h_{ec} they are between 2.37 to 16.63 W/m^2 °C. Consequently, the values of h_c and h_{ec} determined by the theoretical model are below the values reported in the literature. The values of h_c and h_{ec} simulated by the model agree with the behavior of the theoretical T_w, since they were calculated from T_w and T_g according to the equations proposed by Dunkle. That is to say, the heat transfer coefficients are directly proportional to the water and glass temperatures, meaning that the higher T_w and T_g, the higher values of h_c and h_{ec} will be reported by the mathematical model. These parameters directly affect the final productivity of distilled water in the solar still.

Finally, the production rate of distilled water and the efficiency of the solar still, both theoretical and experimental, are shown in Table 7.

Table 7. Theoretical and experimental rates and efficiencies of distilled water production in the solar still.

Parameters	Symbol	Theoretical	Experimental
Daily distillate per unit basin area (Kg/m^2-d)	M'_w	2.367	1.57
Solar still efficiency (%)	η	30.22	20.04

The theoretical and experimental distillation rate, as well as the efficiency of the distiller, showed marked differences. When comparing the M'_w of the solar still in the particular conditions of time and place where the tests were carried out, with the M'_w reported in other sites ($2.0 < M'_w < 5.0$ Kg/m^2 day) [52,53], the experimental rate found in this study is below the expected performance, demonstrating the influence of the climatic factors in the performance of the solar still. Primarily, these factors were the low solar radiation and cloudiness present on the days when the tests were carried out.

4. Conclusions

The average values of solar radiation, relative humidity, cloud cover, and to a great extent, the climatic conditions of the "La Guadalupe" sector on the coast of the Gulf of Mexico are adequate for the operation of a single-slope solar still. However, the solar still performance was affected by the climatic conditions present during the test days, mainly the low solar radiation and the high variability of cloud cover throughout each monitored day. The was due to the occurrence of Hurricane Grace, which hit the region where this study was carried out two days before the start of the experiments. Nonetheless, and although the correlations proposed in the Dunkle model are valid for operating temperatures around 50 °C, the values of the parameters simulated by this mathematical model show an excellent fit and a very good approximation concerning the water temperature values (T_w) recorded experimentally. As a direct consequence of the climatic factors mentioned, M'_w and η achieved in the solar still were also low, even below other production and performance rates reported in other latitudes of the world, demonstrating the significance of the climate factors on the performance of the solar still.

Effluent water from solar still is of excellent quality and could be used in places with high water stress. Nonetheless, complementary physicochemical quality studies must be carried out to identify its potential use as water for human consumption.

Finally, solar stills represent a viable alternative for the solution (on a small scale) of the freshwater deficit in vulnerable populations located in coastal areas, especially those in tropical and developing countries.

References

1. Singh, S.K.; Kaushik, S.C.; Tyagi, V.V.; Tyagi, S.K. Comparative Performance and parametric study of solar still: A review. *Sustain. Energy Technol. Assess.* **2021**, *47*, 101541. [CrossRef]
2. Xiao-jun, W.; Jian-yun, Z.; Shahid, S.; Xing-hui, X.; Rui-min, H.; Man-ting, S. Catastrophe theory to assess water security and adaptation strategy in the context of environmental change. *Mitig. Adapt. Strateg. Glob. Chang.* **2014**, *19*, 463–477. [CrossRef]
3. Shahzad, M.W.; Burhan, M.; Ybyraiymkul, D.; Ng, K.C. Desalination processes' efficiency and future roadmap. *Entropy* **2019**, *21*, 84. [CrossRef] [PubMed]
4. Shatat, M.; Worall, M.; Riffat, S. Opportunities for solar water desalination worldwide: Review. *Sustain. Cities Soc.* **2013**, *9*, 67–80. [CrossRef]
5. Reddy, K.V.K.; Somanchi, N.S.; Kumar, B.S.P.; Banoth, H.B.; Gugulothu, R.; Naveen, B.S. Experimental Investigation on Performance Evaluation of a Single Basin Solar Still Using Different Energy Absorbing Materials. In Proceedings of the ASME 2014, 8th International Conference on Energy Sustainability (ES2014), Boston, MA, USA, 30 June–2 July 2014.
6. Hedayatizadeh, M.; Sarhaddi, F.; Pugsley, A. A detailed thermal modeling of a passive single-slope solar still with improved accuracy. *Groundw. Sustain. Dev.* **2020**, *11*, 100384. [CrossRef]
7. Roy, A.; Pramanick, K. Analysing progress of sustainable development goal 6 in India: Past, present, and future. *J. Environ. Manag.* **2019**, *232*, 1049–1065. [CrossRef]
8. Zhu, S.F.; Xue, L.B.; Xu, Z.D. The development history and an analysis of the status quo of desalination at home and abroad. Technol. *Water Treat.* **2014**, *40*, 12–23.
9. Meteorologica; Aristotle. *The Works of Aristotle*, 3rd ed.; Ross, W.D., Ed.; Webster, E.W., Translator; Clarendon Press: Oxford, UK, 1931; Volume 3, pp. §358:16–18, §359:1–5.
10. Angelakis, A.N.; Valipour, M.; Choo, K.-H.; Ahmed, A.T.; Baba, A.; Kumar, R.; Toor, G.S.; Wang, Z. Desalination: From Ancient to Present and Future. *Water* **2021**, *13*, 2222. [CrossRef]
11. Feria-Díaz, J.J.; López-Méndez, M.C.; Rodríguez-Miranda, J.P.; Sandoval-Herazo, L.C.; Correa-Mahecha, F. Commercial thermal technologies for desalination of water from renewable energies: A state of the art review. *Processes* **2021**, *9*, 262. [CrossRef]
12. Esmaeilion, F. Hybrid renewable energy systems for desalination. *Appl. Water Sci.* **2020**, *10*, 1–47. [CrossRef]
13. Ahmed, F.E.; Hashaikeh, R.; Hilal, N. Hybrid technologies: The future of energy-efficient desalination—A review. *Desalination* **2020**, *495*, 114659.
14. Nassrullah, H.; Anis, S.F.; Hashaikeh, R.; Hilal, N. Energy for desalination: A state-of-the-art review. *Desalination* **2020**, *491*, 114569. [CrossRef]
15. Aybar, H.S.; Assefi, H. A review and comparison of solar distillation: Direct and indirect type systems. *Desalination Water Treat.* **2009**, *10*, 321–331. [CrossRef]
16. Sharshir, S.W.; Yang, N.; Peng, G.; Kabeel, A.E. Factors affecting solar stills productivity and improvement techniques: A detailed review. *Appl. Therm. Eng.* **2016**, *100*, 267–287. [CrossRef]
17. Prakash, P.; Velmurugan, V. Parameters influencing the productivity of solar stills—A review. *Renew. Sustain. Energy Rev.* **2015**, *49*, 585–609. [CrossRef]
18. Muftah, A.F.; Alghoul, M.A.; Fudholi, A.; Abdul-Majeed, M.M.; Sopian, K. Factors affecting basin type solar still productivity: A detailed review. *Renew. Sustain. Energy Rev.* **2014**, *32*, 430–447. [CrossRef]
19. Dunkle, R.V. Solar water distillation: The Roof Type and a Multiple Effect Diffusion Still. In Proceedings of the International Heat Transfer Conference, Boulder, CO, USA, 28 August–1 September 1961; pp. 895–902.
20. Elango, C.; Gunasekaran, N.; Sampathkumar, K. Thermal models of solar still—A comprehensive review. *Renew. Sustain. Energy Rev.* **2015**, *47*, 856–911. [CrossRef]
21. Kumar, S.; Tiwari, G.N. Estimation of convective mass transfer in solar distillation systems. *Sol. Energy* **1996**, *57*, 459–464. [CrossRef]
22. Adhikari, R.S.; Kumar, A.; Kumar, A. Estimation of mass-transfer rates in solar stills. *Int. J. Energy Res.* **1990**, *14*, 737–744. [CrossRef]
23. Congua; Semarnat. *Water Atlas in Mexico*; Semarnat: Mexico City, Mexico, 2018; pp. 8–30. ISBN 2345-4532.

24. Martínez-Austria, P.F.; Díaz-Delgado, C.; Moeller-Chavez, G. Water security in Mexico: General diagnosis and main challenges. *Ing. Agua* **2019**, *23*, 107–121.

25. Jamil, M.A.; Yaqoob, H.; Farooq, M.U.; Teoh, Y.H.; Xu, B.B.; Mahkamov, K.; Sultan, M.; Ng, K.C.; Shahzad, M.W. Experimental Investigations of a Solar Water Treatment System for Remote Desert Areas of Pakistan. *Water* **2021**, *13*, 1070. [CrossRef]

26. Duffie, J.A.; Beckman, W.A.; Worek, W.M. *Solar Engineering of Thermal Processes*, 4th ed.; Wiley and Son: Hoboken, NJ, USA, 2013; Chapter 18; pp. 640–647. ISBN 978-0-470-87366-3.

27. Antar, M.A.; Zubair, S.M. Performance evaluation of a solar still in the Eastern Province of Saudi Arabia—An improved analysis. Desalin. *Water Treat.* **2010**, *22*, 100–110. [CrossRef]

28. Belessiotis, V.; Kalogirou, S.; Delyannis, E. Chapter 3: Solar Distillation-Solar Stills. In *Thermal Solar Desalination: Methods and Systems*, 1st ed.; Elsevier Inc.: New York, NY, USA, 2016; pp. 103–190. ISBN 978-0-12-809656-7.

29. Agrawal, A.; Rana, R.S.; Srivastava, P.K. Heat transfer coefficients and productivity of a single slope single basin solar still in Indian climatic condition: Experimental and theoretical comparison. *Resour.-Effic. Technol.* **2017**, *3*, 466–482. [CrossRef]

30. Sharma, V.B.; Mullick, S.C. Estimation of heat-transfer coefficients, the upward heat flow, and evaporation in a solar still. *J. Sol. Energy Eng. Trans. ASME* **1991**, *113*, 36–41. [CrossRef]

31. Sharma, V.B.; Mullick, S.C. Calculation of hourly output of a solar still. *J. Sol. Energy Eng. Trans. ASME* **1993**, *115*, 231–236. [CrossRef]

32. Kumar, S.; Tiwari, G.N.; Gaur, M.K. Development of empirical relation to evaluating the heat transfer coefficients and frictional energy in basin type hybrid (PV/T) active solar still. *Desalination* **2010**, *250*, 214–221. [CrossRef]

33. Khan, S.; Ali Khan, M.; Zafar, A.; Javed, M.F.; Aslam, F.; Musarat, M.A.; Vatin, N.I. Predicting the Ultimate Axial Capacity of Uniaxially Loaded CFST Columns Using Multiphysics Artificial Intelligence. *Materials* **2022**, *15*, 39. [CrossRef]

34. Aldrees, A.; Khan, M.A.; Tariq, M.A.U.R.; Mustafa Mohamed, A.; Ng, A.W.M.; Bakheit Taha, A.T. Multi-Expression Programming (MEP): Water Quality Assessment Using Water Quality Indices. *Water* **2022**, *14*, 947. [CrossRef]

35. Khatri, P.; Kumar-Gupta, K.; Kumar-Gupta, R. Raspberry Pi-based smart sensing platform for drinking-water quality monitoring system: A Python framework approach. *Drink. Water Eng. Sci.* **2019**, *12*, 31–37. [CrossRef]

36. Alade, I.O.; Bagudu, A.; Oyehan, T.A.; Abd Rahman, M.A.; Saleh, T.A.; Olatunji, S.O. Estimating the refractive index of oxygenated and deoxygenated hemoglobin using a genetic algorithm–support vector regression model. Comput. *Methods Programs Biomed.* **2018**, *163*, 135–142. [CrossRef] [PubMed]

37. Nafees, A.; Amin, M.N.; Khan, K.; Nazir, K.; Ali, M.; Javed, M.F.; Aslam, F.; Musarat, M.A.; Vatin, N.I. Modeling of Mechanical Properties of Silica Fume-Based Green Concrete Using Machine Learning Techniques. *Polymers* **2022**, *14*, 30. [CrossRef]

38. Turner, J.R.; Thayer, J.F. *Introduction to Analysis of Variance: Design, Analysis, and Interpretation*, 1st ed.; SAGE Publications: New York, NY, USA, 2001; ISBN 978-0803970755.

39. Mongomery, D.C. *Design and Analysis of Experiments*, 10th ed.; John Willy & Sons: Hoboken, NJ, USA, 2019; ISBN 978-1-119-49244-3.

40. Hasanah, R.N.; Indyanto, F.R.; Maulana, E.; Suyono, H. Solar Energy Hybrid System for Seawater Distillation in the Coastal Regions. *Energy Procedia* **2017**, *143*, 662–667. [CrossRef]

41. Gorjian, S.; Ghobadian, B.; Tavakkoli Hashjin, T.; Banakar, A. Experimental performance evaluation of a stand-alone point-focus parabolic solar still. *Desalination* **2014**, *352*, 1–17. [CrossRef]

42. Lawrence, M.G. The relationship between relative humidity and the dewpoint temperature in moist air: A simple conversion and applications. Bull. *Am. Meteorol. Soc.* **2005**, *86*, 225–233. [CrossRef]

43. Abujazar, M.S.S.; Fatihah, S.; Rakmi, A.R.; Shahrom, M.Z. The effects of design parameters on the productivity performance of a solar still for seawater desalination: A review. *Desalination* **2016**, *385*, 178–193. [CrossRef]

44. Lindblom, J.; Nordell, B. Water production by underground condensation of humid air. *Desalination* **2006**, *189*, 248–260. [CrossRef]

45. Kalidasa Murugavel, K.; Anburaj, P.; Samuel Hanson, R.; Elango, T. Progresses in inclined type solar stills. *Renew. Sustain. Energy Rev.* **2013**, *20*, 364–377. [CrossRef]

46. Zamfir, E.; Oancea, C.; Badescu, V. Cloud cover influence on long-term performances of flat plate solar collectors. *Renew. Energy* **1994**, *4*, 339–347. [CrossRef]

47. World Health Organization. *Guidelines for Drinking-Water Quality*, 4th ed.; WHO: Geneva, Switzerland, 2017; Chapter 10; pp. 219–230, ISBN 978-92-4-154995-0.

48. Mowla, D.; Karimi, G. Mathematical modeling of solar stills in Iran. *Sol. Energy* **1995**, *55*, 389–393. [CrossRef]

49. Salina-Freire, H.A.; Pérez-Ones, O.; Rodríguez-Muños, S. Thermodinamical productivity limitations for passive solar stills. *Rev. ION* **2019**, *32*, 7–20.

50. Tiwari, G.N.; Sahota, L. Advanced Solar-Distillation Systems: Basic Principles, Thermal Modeling, and Its Application. In *Green Energy and Technology*, 1st ed.; Springer Nature: Singapore, 2017; p. 427.

51. Kabeel, A.E.; Omara, Z.M.; Essa, F.A. Numerical investigation of modified solar still using nanofluids and external condenser. *J. Taiwan Inst. Chem. Eng.* **2017**, *75*, 77–86. [CrossRef]

52. Kalidasa-Murugavel, K.; Chockalingam, K.K.S.K.; Srithar, K. Progresses in improving the effectiveness of the single basin passive solar still. *Desalination* **2008**, *220*, 677–686. [CrossRef]

53. Durkaieswaran, P.; Murugavel, K.K. Various special designs of single basin passive solar still—A review. *Renew. Sustain. Energy Rev.* **2015**, *49*, 1048–1060. [CrossRef]